Research Article

Electrospun Cu-doped In$_2$O$_3$ hollow nanofibers with enhanced H$_2$S gas sensing performance

Yu ZHANG^{a,†}, Shuai HAN^{a,†}, Mingyuan WANG^{b,†}, Siwei LIU^{a}, Guiwu LIU^{a,*}, Xianfeng MENG^{a}, Ziwei XU^{a}, Mingsong WANG^{a}, Guanjun QIAO^{a}

^{a}*School of Materials Science and Engineering, Jiangsu University, Zhenjiang 212013, China*
^{b}*SEU-FEI Nano-Pico Center, Key Laboratory of MEMS of Ministry of Education, School of Electrical Science and Engineering, Southeast University, Nanjing 210096, China*

Abstract: One-dimensional nanofibers can be transformed into hollow structures with larger specific surface area, which contributes to the enhancement of gas adsorption. We firstly fabricated Cu-doped In$_2$O$_3$ (Cu–In$_2$O$_3$) hollow nanofibers by electrospinning and calcination for detecting H$_2$S. The experimental results show that the Cu doping concentration besides the operating temperature, gas concentration, and relative humidity can greatly affect the H$_2$S sensing performance of the In$_2$O$_3$-based sensors. In particular, the responses of 6%Cu–In$_2$O$_3$ hollow nanofibers are 350.7 and 4201.5 to 50 and 100 ppm H$_2$S at 250 ℃, which are over 20 and 140 times higher than those of pristine In$_2$O$_3$ hollow nanofibers, respectively. Moreover, the corresponding sensor exhibits excellent selectivity and good reproducibility towards H$_2$S, and the response of 6%Cu–In$_2$O$_3$ is still 1.5 to 1 ppm H$_2$S. Finally, the gas sensing mechanism of Cu–In$_2$O$_3$ hollow nanofibers is thoroughly discussed, along with the assistance of first-principles calculations. Both the formation of hollow structure and Cu doping contribute to provide more active sites, and meanwhile a little CuO can form p–n heterojunctions with In$_2$O$_3$ and react with H$_2$S, resulting in significant improvement of gas sensing performance. The Cu–In$_2$O$_3$ hollow nanofibers can be tailored for practical application to selectively detect H$_2$S at lower concentrations.

Keywords: electrospinning; Cu-doped In$_2$O$_3$; hollow nanofibers; H$_2$S detection

1 Introduction

Hydrogen sulfide (H$_2$S) is a highly toxic reducing gas, which can pose major hazards to the living environment and health of human being. The main sources of H$_2$S gas are oil and gas wells, crude oil refining, coal gasification plants, decomposition of sulfur-containing organic matter, and food processing industries [1–3]. Continuous exposure to H$_2$S at a concentration of over 10 ppm will cause serious health hazards, such as coma, severe poisoning, rapid apnea, and inactivation of the olfactory system, etc. [4,5]. If the H$_2$S concentration exceeds 250 ppm, it will endanger life and even bring about death [6,7]. Therefore, the effective detection and monitoring of H$_2$S is particularly important, so that it poses a great challenge for researchers to develop high-performance H$_2$S sensors.

† Yu Zhang, Shuai Han, and Mingyuan Wang contributed equally
  to this work.
* Corresponding author.
E-mail: gwliu76@ujs.edu.cn

In recent years, metal oxide semiconductors (MOSs), such as ZnO, In_2O_3, SnO_2, TiO_2, CuO, and WO_3 [8–13], have been widely used for detecting various gases (involving NO_2 [14], CO [15], H_2S [16], Cl_2 [17], ethanol [18], acetone [19], etc.) due to the advantages of high sensitivity, good selectivity, fast response and recovery characteristics, and long-term stability [20]. Among them, In_2O_3, as a typical n-type semiconductor material, possesses high sensitivity and selectivity in the detection of H_2S owing to its wide bandgap of ~3.6 eV, good electrical conductivity, and excellent catalytic activity [1,3,21]. Considering that In_2O_3 is suitable for gas sensors, there are demands for more accurate response to the gas to be detected and improved selectivity in identifying the target gas. According to the previous reports, there are three main technical means to enhance the gas sensing performance of In_2O_3: (i) modulating the material morphology to achieve larger specific surface area [22,23]; (ii) elemental doping to cause changes in the grain size and energy band structure of the material [24,25]; (iii) compounding with other semiconductor materials to build heterogeneous structures [26,27]. Actually, all the three aspects are essentially designed to provide more active sites. For instance, Wei *et al.* [25] synthesized La-doped In_2O_3 (La–In_2O_3) hollow microspheres using a hydrothermal process, and obtained the highest response of 17.8 to 10 ppm H_2S, which is approximately 4.8 times higher than that of pristine In_2O_3 at 200 ℃. Li *et al.* [27] fabricated a bamboo-like CuO/In_2O_3 heterostructure via a solvothermal method, and achieved the response of 229.3 to 5 ppm H_2S, which can be mainly attributed to the severe sulfation of CuO by H_2S, as a result of that the resistance value cannot be restored naturally. At present, the related investigations on In_2O_3-based H_2S gas sensors are still not extensive, and some H_2S sensors present the disadvantages of low sensitivity, difficulty in recovering the resistance, and poor stability. Especially for the H_2S sensors with high response value, the complete recovery mostly requires a thermal pulse assistance or high temperature environment exceeding 500 ℃ [27,28]. Hence, further explorations are needed to solve these problems.

The options of material morphology and additives are particularly critical for the enhancement of gas sensing performance. The hollow nanofibers or nanotubes are gradually attracting the attention of researchers, since these hollow structures with high aspect ratio show excellent promise for gas sensing application. For instance, Zeng *et al.* [23] synthesized pearl-necklace-shaped In_2O_3 nanotubes by electrospinning and calcination, indicating a higher response of 38.3 to 100 ppm formaldehyde, and the shorter response and recovery time (6 and 16 s, respectively) compared with the corresponding non-hollow In_2O_3 nanofibers. Noted that the p-type CuO-based H_2S sensors can show the enhanced sensing performance by establishing p–n heterojunctions and sulfation reaction. For instance, Park *et al.* [29] synthesized highly porous SnO_2–CuO hollow nanofibers using a combination of electrospinning and annealing, showing an extremely high response of 1395 to 5 ppm H_2S at 200 ℃ and short response time of about 5.27 s. In short, hollow nanofibers are of great significance for the improvement of gas sensing performance, and especially few investigations on H_2S sensor based on In_2O_3 hollow nanofibers were explored.

In this study, pristine In_2O_3 and Cu-doped In_2O_3 (Cu–In_2O_3) hollow nanofibers were prepared by electrospinning and calcination. The Cu doping concentration and the operating temperature of the sensor were optimized to improve its gas sensing performance to H_2S. The as-fabricated pristine In_2O_3 and Cu–In_2O_3 hollow nanofibers were eventually used to detect H_2S gas at concentrations of 1–100 ppm at 150–300 ℃. Meanwhile, the selectivity of 6%Cu–In_2O_3 to H_2S was investigated experimentally. Finally, the mechanism of gas sensitivity enhancement of Cu–In_2O_3 hollow nanofibers was discussed by incorporating the first-principles calculations. The Cu–In_2O_3 hollow nanofiber sensor can achieve high response to H_2S, and its excellent sensing performance will increase potential as an efficient candidate for gas sensors. Likewise, our work overcomes the problem that it is difficult for H_2S gas sensors with high response to recover naturally.

2　Experimental

2.1　Chemical reagents

All the chemicals, involving indium nitrate ($In(NO_3)_3$· $4.5H_2O$), copper nitrate trihydrate ($Cu(NO_3)_2$·$3H_2O$), N,N-dimethylformamide (DMF), and polyvinylpyrrolidone (PVP) ($M_w = 1,300,000$), were obtained commercially from Sinopharm Chemical Reagent Co., Ltd. and Aladdin Chemistry Co., Ltd., which were of analytical-reagent grade and directly used without any purification.

2.2 Preparation of pristine In_2O_3 and $Cu–In_2O_3$ hollow nanofibers

The pristine In_2O_3 hollow nanofibers were prepared by a combination of electrospinning and calcination processes. $In(NO_3)_3 \cdot 4.5H_2O$ (0.4 g) was firstly dissolved in a solution composed of ethanol (5.5 mL) and DMF (4.5 mL) by stirring for 30 min to obtain a homogeneous electrospun solution, and then PVP (0.8 g) was added into the above solution and stirred vigorously at room temperature for 12 h. Subsequently, the as-prepared precursor solution was moved into a 10 mL syringe using a stainless steel needle of Ø0.4 mm. The voltage was maintained at 15 kV during the spinning process, the distance between the needle tip and the collector was ~15 cm, and the injection rate of the syringe was 0.6 mL/h. After electrospinning, the nanofibers on the silicone oil paper were collected and then dried at 60 ℃ for 12 h. Finally, the as-obtained nanofibers were calcined at 500 ℃ for 2 h in air.

The preparation of $x\%Cu–In_2O_3$ (x = 2, 4, 6, 8) hollow nanofibers was performed by an identical process to that of pristine In_2O_3 hollow nanofibers except the different addition amount of $Cu(NO_3)_2 \cdot 3H_2O$ together with $In(NO_3)_3 \cdot 4.5H_2O$, where x is the nominal molar ratio of Cu to In. Figure 1 shows the schematic of preparation and formation of $Cu–In_2O_3$ hollow nanofibers.

2.3 Material characterization

The crystal structures and phase composition of the as-fabricated nanofibers were characterized by X-ray diffraction (XRD; Bruker D8 Advance, Cu Kα, λ = 1.5418 Å) in the 2θ range of 15°–70°. The structures of pristine In_2O_3 and $x\%Cu–In_2O_3$ were refined based on the In_2O_3 (ICSD Code #14387) model using the Rietveld type method supported by the FullProf software, as a result of that the corresponding lattice constants can be

obtained. The morphologies and microstructures of the as-fabricated materials were observed and analyzed by scanning electron microscopy (SEM; FEI, Nova Nano 450) and high-resolution transmission electron microscopy (HRTEM; JEOL JEM 2100F, 200 kV) coupled with selected area electron diffraction (SAED) and energy-dispersive spectroscopy (EDS). The N_2 adsorption–desorption isotherms were acquired using an adsorption instrument (Micrometrics, ASAP 2460), and the specific surface area was calculated by the Brunauer–Emmett–Teller (BET) method. X-ray photoelectron spectroscopy (XPS; Thermo Scientific K-Alpha) measurements were performed for surface element analysis.

2.4 Gas-sensor fabrication and performance test

The as-fabricated pristine In_2O_3 and $x\%Cu–In_2O_3$ nanofibers (~2 mg) were uniformly dispersed in ethanol (50 μL) by ultrasonic vibration for 30 min, and then a pipette (10 μL) was used to apply the resulting pastes on the surfaces of alumina substrates (i.e., Pt-coated alumina electrodes). Here, the Pt-coated alumina electrodes were purchased from Wuhan Huachuang Ruike Technology Co., Ltd., China. Afterwards, the nanofiber-coated substrates were dried in an oven for 60 min to remove ethanol, and aged in a furnace at 250 ℃ for 24 h to improve the stability of the sensitive materials. The as-obtained substrates were put into the dynamic four-channel gas sensor test system (SD101) to test the performance index of the gas sensors towards the target gases. The gas sensor test system consists of five components: gases source, test electrodes, a four-channel co-mingled gas flow control module, an aluminum alloy test chamber, and a data acquisition system, as shown in Fig. S1 in the Electronic Supplementary Material (ESM). Here, N_2 serves as the base gas for 100 ppm target gases (H_2S, NO_2, NH_3, and SO_2) in the measurement.
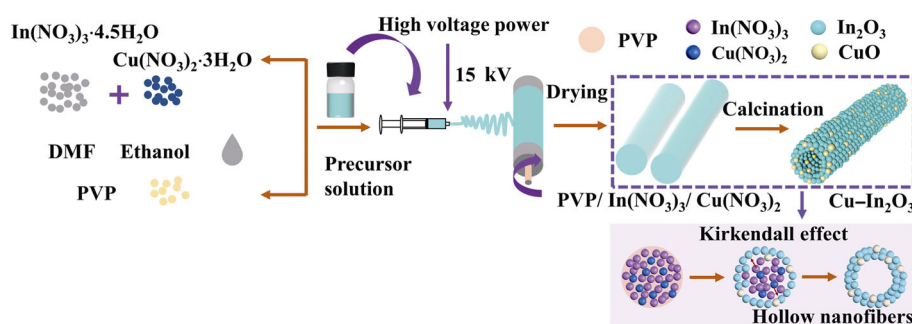

Fig. 1 Schematic of preparation and formation of $Cu–In_2O_3$ hollow nanofibers.

According to the formula $\rho = m/v$, the stacking density of pristine In_2O_3 and Cu–In_2O_3 hollow nanofibers on the electrode is estimated to be ~0.64 g/cm³, where ρ is the stacking density, m is the mass of nanofiber coating on the electrode, and v is the volume of the coating. Typically, for an n-type semiconductor the response (R) of a sensor is specified as R_a/R_g, and the response/recovery time (τ_{res}/τ_{rec}) is defined as the one required for 90% change in sensor resistance in the target gas and air, respectively.

2.5 Computational method

In this work, all the calculations were performed based on the density functional theory (DFT) as implemented in the VASP code [30]. The Perdew–Burke–Ernzerhof (PBE) of generalized gradient approximation (GGA) was chosen as the exchange–correction functional [31]. The kinetic energy cutoff was selected to be 450 eV and a $3 \times 3 \times 1$ k-points mesh was sampled. A vacuum space of $\geqslant$ 30 Å was set in the unit cell to minimize the interactions of the system and its replicas derived from the periodic boundary conditions [32]. The van der Waals interactions were amended by analyzing the interactions of pristine In_2O_3 or 6%Cu–In_2O_3 nanofibers with gas molecules using vdW-D3 [33]. All the atomic structures were completely relaxed until the force on each atom was less than 0.01 eV/Å. The energy convergence criteria were set to be 10^{-4} eV. After structure optimization, the unit cell parameters of pristine In_2O_3 were $a = 14.60$ Å, $b = 14.60$ Å, $c = 30$ Å, $\alpha = 90.00°$, $\beta = 90.0099°$, $\gamma = 120.00°$. To be basically consistent with the experiment and ensure the accuracy and validity of calculation, the (111) surface of In_2O_3 ($In_{48}O_{72}$) was adopted and the 6%Cu–In_2O_3 structure was $In_{45}Cu_3O_{72}$. The adsorption energy (E_{ads}) was calculated using Eq. (1) [34]:

$$E_{ads} = E_{gas@slab} - E_{slab} - E_{gas} \qquad (1)$$

where $E_{gas@slab}$, E_{slab}, and E_{gas} are the energies of the total system (gas adsorbed on the slab, pristine In_2O_3 or 6%Cu–In_2O_3), the slab of pristine In_2O_3 or 6%Cu–In_2O_3, and the adsorbed gas molecules, respectively.

3 Results and discussion

3.1 Structure and morphology

Figure 2(a) shows the XRD patterns of pristine In_2O_3 and Cu–In_2O_3 hollow nanofibers. The XRD patterns of all the samples well correspond to the characteristic peaks of cubic In_2O_3 (JCPDS No. 06-0416), and no peaks derived from Cu-related compounds are observed as the amount of Cu doping is below 6%. This is due to the fact that most of the Cu^{2+} ions enter the In_2O_3 lattice to cause lattice distortion, without formation of new products. On the other hand, it is difficult to detect the low concentration of CuO by the X-ray diffraction. However, a visible characteristic peak (111) of CuO except the (002) appears while introducing 8% Cu^{2+}. Moreover, the main diffraction peak indexed to the (222) crystal plane of the Cu–In_2O_3 hollow nanofibers shifts slightly toward the larger diffraction angle compared with the XRD pattern of pristine In_2O_3 hollow nanofibers (Fig. 2(b)). This is because Cu^{2+} (0.72 Å) with a smaller ion radius enters into the In_2O_3 lattice instead of In^{3+} (0.81 Å) ions with a larger ion radius, which can cause the lattice spacing to shrink, resulting in the lattice contraction. The Rietveld refinement profile for 6%Cu–In_2O_3 based on the cubic crystal structure (space group, $Ia\overline{3}$) reveals that the final agreement factors converge to R_p 10.5%, R_{wp} 11.8%, and R_{exp} 4.55% (Fig. 2(c)). The lattice constant decreases monotonously with the Cu doping concentration increasing (Fig. 2(d)), and the similar results were reported [35,36]. The above results indicate that a large portion of Cu^{2+} ions is doped into the In_2O_3 lattice and a small portion is applied to generate CuO.

The SEM images of pristine In_2O_3 and x%Cu–In_2O_3 hollow nanofibers indicate the hollow structure, as shown in Fig. 3. The surface rough of In_2O_3 hollow nanofibers is gradually decreased with the Cu doping concentration increasing from 0 to 8%, and the 8%Cu–In_2O_3 hollow nanofibers are broken into the shorter ones with visible fracture (Fig. 3(f)). Meanwhile, the diameter and wall thickness of In_2O_3 hollow nanofibers decrease in varying degrees with the Cu doping concentration increasing. In particular, the diameters and average wall thickness of pristine In_2O_3 hollow nanofibers are of ~200–400 nm and 20 nm, respectively, and the diameter of 6%Cu–In_2O_3 hollow nanofibers is ~150–180 nm. Hence, the doping of Cu can reduce the diameter of In_2O_3 nanofibers. Actually, the finer hollow nanofibers can provide more adsorption sites for gas, which is more conducive to the improvement of gas sensitivity. The formation of the hollow structure is due to the Kirkendall effect that occurs during the heat treatment, where atoms are exchanged with vacancies
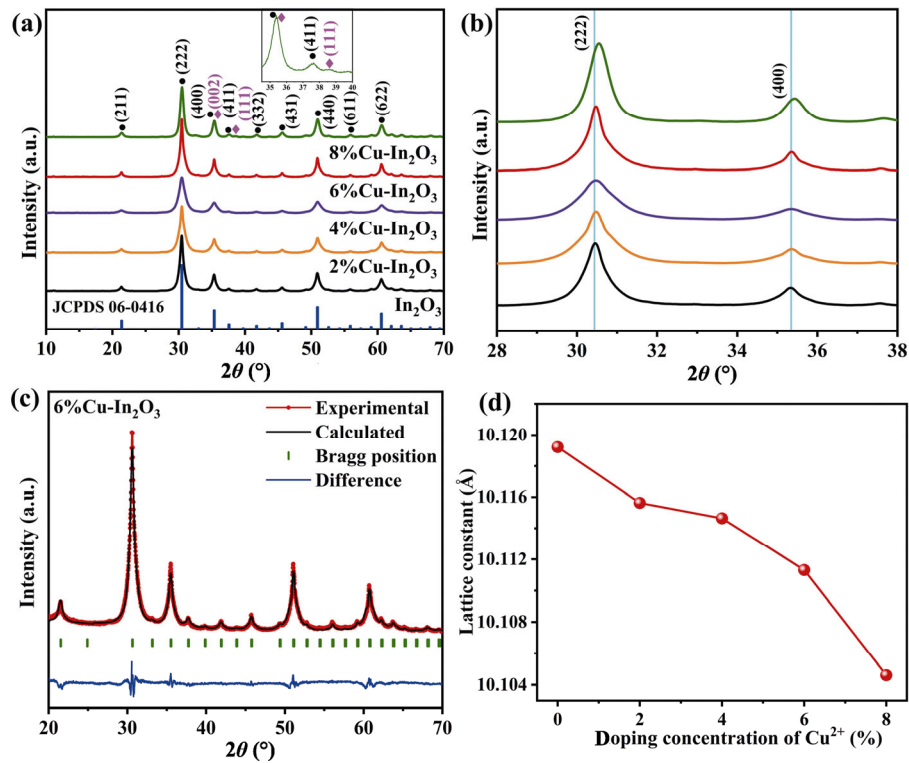
Fig. 2 (a) XRD patterns of pristine In_2O_3 and $Cu–In_2O_3$ nanofibers with various Cu doping concentrations. (b) Enlarged XRD patterns at 2θ of 28°–38°. (c) Rietveld refinement profile for 6%Cu–In_2O_3. (d) Variation of lattice constant with the Cu doping concentration.
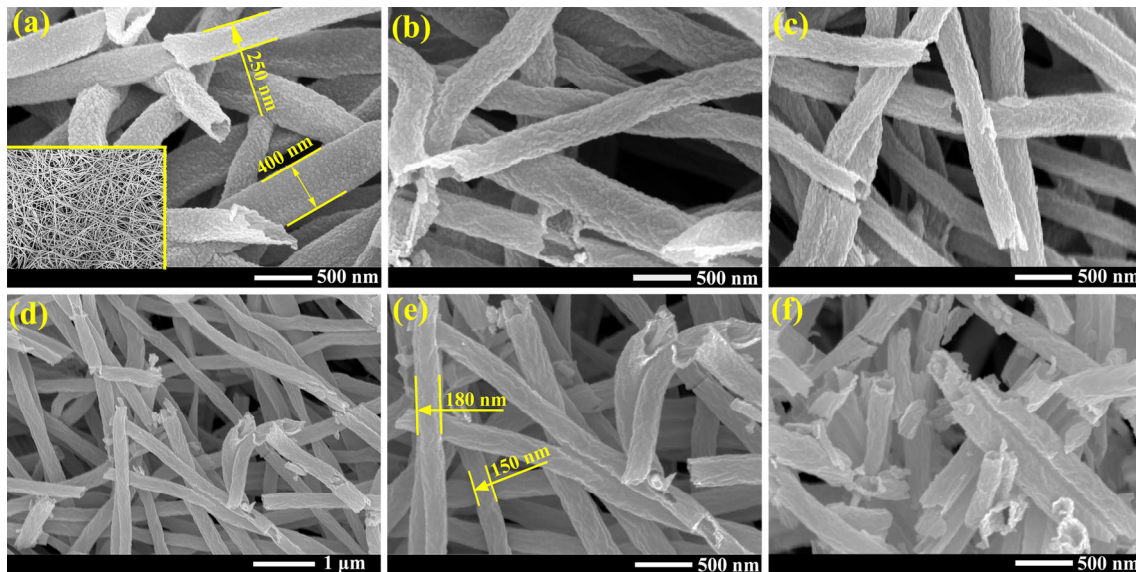

Fig. 3 SEM images of (a) pristine In_2O_3, (b) 2%Cu–In_2O_3, (c) 4%Cu–In_2O_3, (d, e) 6%Cu–In_2O_3, and (f) 8%Cu–In_2O_3 hollow nanofibers. The SEM image at lower left corner of (a) denotes the pristine In_2O_3 precursor nanofibers before calcination.

after the removal of PVP, with In and Cu atoms forming In_2O_3 and CuO, and diffusing rapidly toward the surface [29,37], as shown in Fig. 1. On the other hand, the formation of the hollow structure is also related to the rate of temperature increase. Actually, the high rate of

temperature increase can cause the high decomposition rate of PVP. The rate of gas release is greater than that of gas diffusion through the fiber surface as the decomposition rate of PVP is higher, so that the increase of internal pressure of the fiber is higher than that of

the external pressure, resulting in the formation of hollow nanofibers [38].

The 6%Cu–In$_2$O$_3$ hollow nanofibers were further characterized by using HRTEM, SAED, and EDS mapping, as shown in Fig. 4. The HRTEM image (Fig. 4(b)) reveals that the lattice fringe spacings of 0.29 and 0.41 nm correspond to the (222) and (211) crystal planes of In$_2$O$_3$, respectively. Based on the previous reports [27,36], the crystal plane corresponding to a lattice fringe spacing of 0.25 nm is the CuO (002). The SADE pattern (Fig. 4(c)) corresponds to the (211), (222), (400), (332), (431), (440), (622), (741), and (844) crystal planes of In$_2$O$_3$ and the (002) and ($\bar{4}$22) crystal planes of CuO, which can be attributed to the fact that excessive Cu^{2+} ions diffuse into the surface of In$_2$O$_3$ hollow nanofibers to form CuO nanoparticles. The EDS

elemental mapping results indicate the homogeneous distribution of In, O, and Cu elements in the Cu-doped hollow nanofibers (Figs. 4(e)–4(g)).

Figure 5 shows the nitrogen adsorption–desorption isotherms and BJH pore size distributions of pristine In$_2$O$_3$ and 6%Cu–In$_2$O$_3$ hollow nanofibers. The calculated specific surface area of 6%Cu–In$_2$O$_3$ nanofibers is 71.6 m^2/g, which is higher than that of pristine In$_2$O$_3$ nanofibers (60.7 m^2/g). Note that this specific surface area value is much larger than those (< 40 m^2/g) of other In$_2$O$_3$-based hollow nanofibers or nanotubes [39–41]. The pore sizes (calculated by BJH equation) on the walls of pristine In$_2$O$_3$ and 6%Cu–In$_2$O$_3$ nanofibers are distributed in ~2–55 and 2–70 nm, respectively (insets of Fig. 5), indicating that the Cu doping can cause the slight enlargement of pore on the wall.
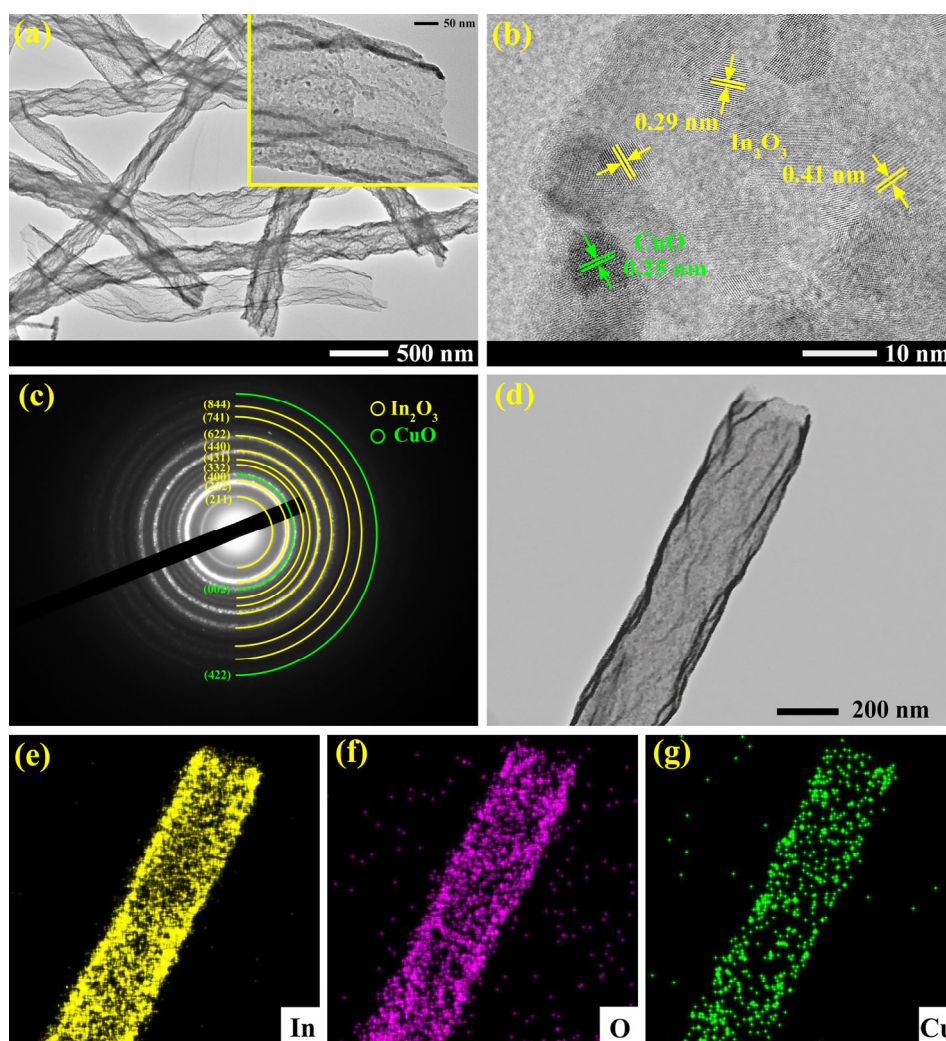

Fig. 4 (a, d) TEM and (b) HRTEM images, and the corresponding (c) SAED pattern and (e–g) EDS elemental mapping of 6%Cu– In$_2$O$_3$ hollow nanofibers.

To examine the surface elemental compositions and chemical states of the pristine In_2O_3 and 6%Cu–In_2O_3 hollow nanofibers, XPS analysis was performed, as shown in Fig. 6. The two survey spectra show that the pristine In_2O_3 nanofibers are only composed of In, O, and C elements, while there is also Cu element in 6%Cu–In_2O_3 nanofibers, which further proves the presence of Cu element (Fig. 6(a)). In the spectra of In 3d (Fig. 6(b)), the peak positions of In $3d_{5/2}$ and In $3d_{3/2}$ move from 444.38 to 444.48 eV and from 451.98 to 452.08 eV after the Cu doping, respectively, due to the electron transfer from In_2O_3 to CuO [26]. For the O 1s spectra (Fig. 6(c)), three fitting peaks can be obtained by Gauss fitting, and these binding energies are located at 530.09, 531.21, and 532.49 eV for pristine In_2O_3 and 530.19, 531.55, and 532.73 eV for 6%Cu–In_2O_3, which can be assigned to lattice oxygen (O_L), oxygen vacancy (O_V), and chemically adsorbed oxygen (O_C), respectively [38]. The percentages of O_L, O_V, and O_C in the pristine In_2O_3 are 34.30%, 20.51%, and 45.19%, while those of O_L, O_V, and O_C in the 6%Cu–In_2O_3 are 34.48%, 36.80%, and 28.72%, respectively,
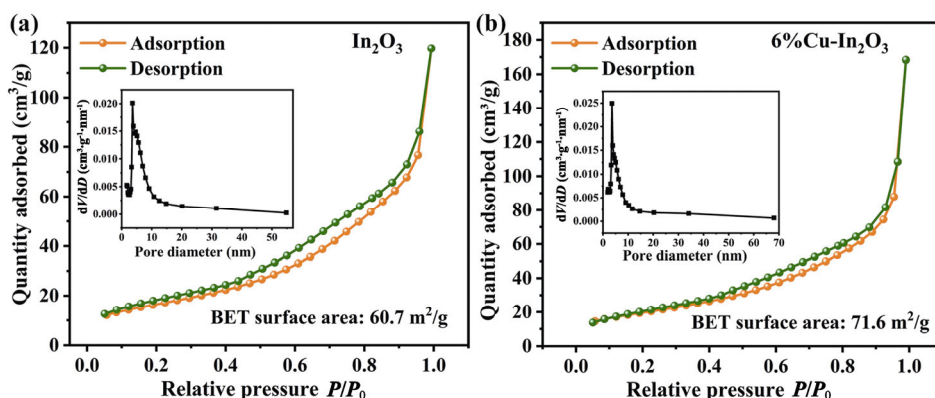

Fig. 5 Nitrogen adsorption–desorption isotherms and pore size distributions of (a) pristine In_2O_3 and (b) 6%Cu–In_2O_3 hollow nanofibers.
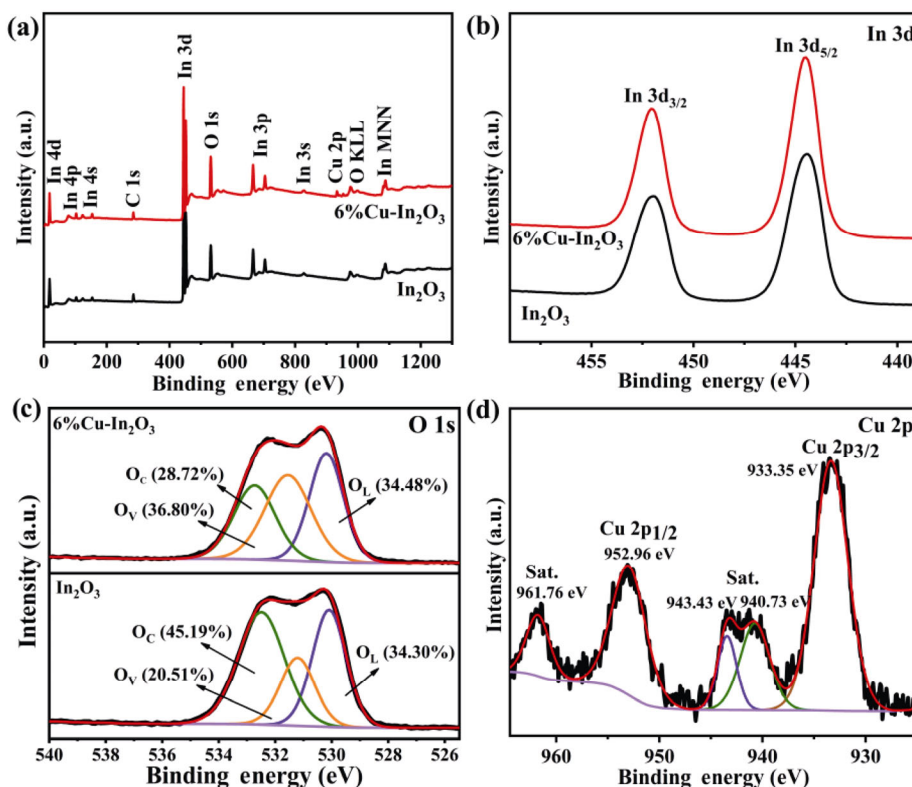

Fig. 6 XPS spectra of pristine In_2O_3 and 6%Cu–In_2O_3 hollow nanofibers: (a) survey, (b) In 3d, (c) O 1s, and (d) Cu 2p.

indicating that the number of oxygen vacancies in the $6\%Cu–In_2O_3$ nanofibers is higher than that in the pristine In_2O_3 nanofibers. The increased oxygen vacancies can provide much more adsorption sites, thus enhancing the sensitivity of the sensor [41,42]. The binding energies of Cu 2p peak (Fig. 6(d)) are around 933.35 and 952.96 eV, corresponding to Cu $2p_{3/2}$ and Cu $2p_{1/2}$, respectively, with the binding energy difference of ~19.61 eV. Furthermore, there are strong satellite peaks of Cu^{2+}, demonstrating that the Cu element exists in the form of Cu^{2+} [27].

3. 2   Gas sensing properties

As we know, the operating temperature is one of the crucial indexes to evaluate the performance for MOS-based gas sensors, and it can highly affect the adsorption and desorption of gases and surface interactions. To determine the optimum operating temperature, the pristine In_2O_3 and $Cu–In_2O_3$ hollow nanofibers were tested for response to 100 ppm H_2S at 150–300 ℃, as shown in Fig. 7(a). Obviously, the optimum operating temperature is 250 ℃, and the responses of $Cu–In_2O_3$ nanofiber based sensors to H_2S are far higher than that of pristine In_2O_3 nanofibers within the test temperature range. In particular, the response of $6\%Cu–In_2O_3$ nanofiber based sensor is the highest (4201.5) while employing the optimum operating temperature, which is over 100 times higher than that of pristine In_2O_3 (29.3). The responses of all the sensors to H_2S gradually increase with the temperature increasing from 150 to 250 ℃, and then decrease with the temperature increasing from 250 to 300 ℃. This is because the gas adsorption capacity becomes weaker at higher temperatures, allowing for easy desorption before surface reactions occur, as a result of that the response decreases in varying degrees with the further increase of temperature [43].

The responses of pristine In_2O_3 and $6\%Cu–In_2O_3$ nanofiber based sensors to H_2S at different concentrations (1–100 ppm) were also investigated at 250 ℃, and the dynamic response/recovery curves are shown in Figs. 7(b) and 7(c). As expected, the response increases with the gas concentration increasing. The responses of pristine In_2O_3 and $6\%Cu–In_2O_3$ based sensors to 1, 3, 5, 10, 20, 50, 80, 100 ppm H_2S are 1.2, 1.5, 1.7, 2.8, 5.6, 14.04, 19.8, 29.3 and 1.5, 4.2, 9, 15.1, 46.22, 316.7, 862.2, 4201.5, respectively. Especially, the responses of $6\%Cu–In_2O_3$ based sensor to 50 and 100 ppm H_2S are ~22 and 143 times higher than those of pristine In_2O_3 (Fig. S2 in the ESM). The resistance of $6\%Cu–In_2O_3$ is significantly

higher than that of the pristine In_2O_3, which is conducive to the increase of response. It is difficult for the resistance to recover after the pristine In_2O_3 interacts with H_2S, leading to the decreasing resistance with the increase of gas concentration. Although the resistance of $6\%Cu–In_2O_3$ nanofiber based sensor can be restored, it takes a long time, namely that the recovery time is over 400 s at 100 ppm.

Figure 7(d) presents the response versus gas concentration for the pristine In_2O_3 and $6\%Cu–In_2O_3$ hollow nanofiber based sensors. For the pristine In_2O_3 based sensors, the response shows a linear relationship with the concentration of H_2S. However, for $6\%Cu–In_2O_3$ based sensors, the response is increased dramatically after 20 ppm, which is mainly related to the reversible chemical reaction of CuO with H_2S [44], the role of oxygen vacancy, and the reaction of surface oxygen ions with H_2S, as discussed below. Figure 7(e) shows their variations of response time with the H_2S concentration, where the response time is calculated from the two dynamic curves (Figs. 7(b) and 7(c)). As expected, the response time decreases with the gas concentration increasing, and the response time of the $6\%Cu–In_2O_3$ based sensor is significantly less than that of the pristine In_2O_3 at each concentration of H_2S. The response time of the $6\%Cu–In_2O_3$ is 24 and 18 s while employing 50 and 100 ppm H_2S, which is 20 and 12 s less than that of the pristine In_2O_3 based sensor, respectively (Fig. S2 in the ESM). The response and recovery time of $6\%Cu–In_2O_3$ based sensor for 1 ppm H_2S is ~125 and 175 s, respectively. Moreover, the response time is shortened rapidly as the gas concentration exceeds 5 ppm.

Good selectivity is one of the basic requirements for a gas sensor to avoid the interference of other gases during the sensing process. To investigate their selectivity, the responses of pristine In_2O_3 and $6\%Cu–In_2O_3$ based sensors to 100 ppm H_2S and other gases, involving NO_2, NH_3, SO_2, ethanol, and acetone, were recorded at 250 ℃. It reveals that the response (4201.5) of $6\%Cu–In_2O_3$ based sensor to H_2S is remarkably superior to other gases, exhibiting excellent selectivity (Fig. 7(f)).

We also checked the current−voltage (*I*−*V*) characteristics of $6\%Cu–In_2O_3$ based sensor at various temperatures in air. As shown in Fig. S3 in the ESM, the *I*−*V* curves of $6\%Cu–In_2O_3$ are linear, indicating the formation of ohmic contact between the $6\%Cu–In_2O_3$ and Pt electrode [44]. Moreover, the reciprocal of slope (i.e., resistance) decreases with the temperature
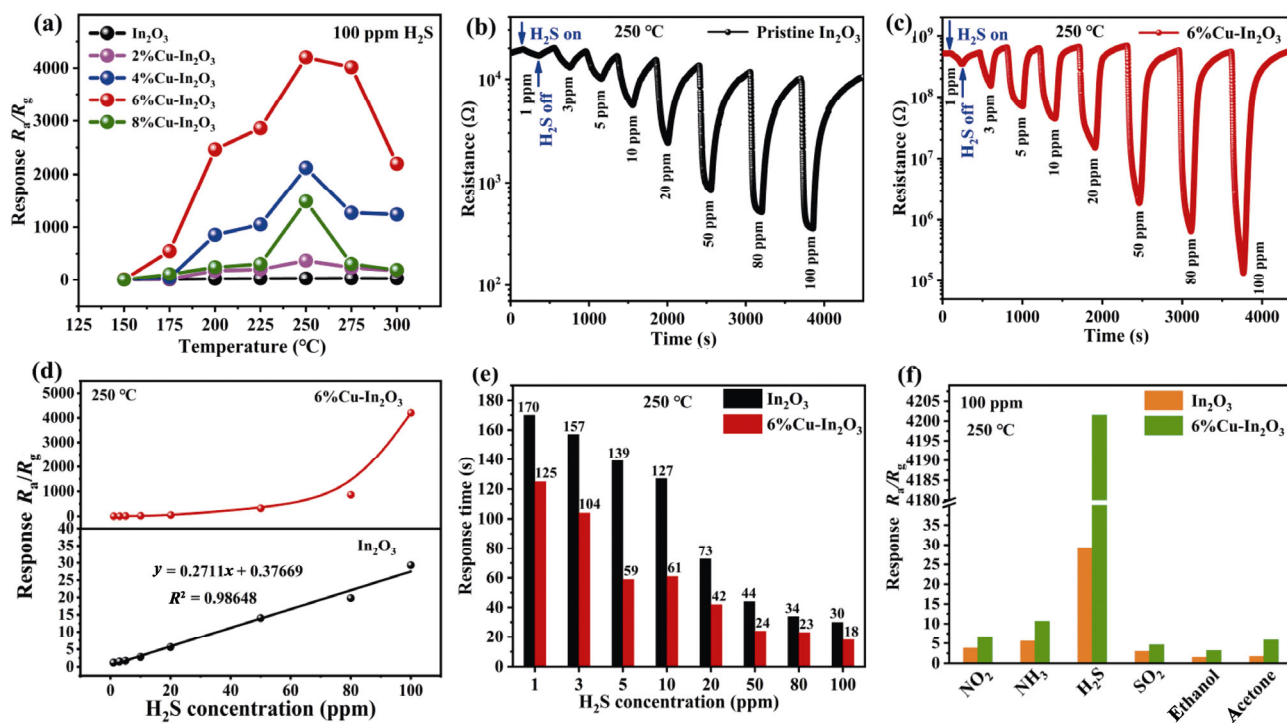
Fig. 7 (a) Responses to 100 ppm H_2S at various operating temperatures. (b, c) Dynamic response and recovery curves for 1–100 ppm H_2S. (d) Fitting curves of response to H_2S concentration. (e) Response time at different H_2S concentrations. (f) Selectivity to various gases of pristine In_2O_3 and 6%Cu–In_2O_3 hollow nanofiber based sensors.

increasing, which is in good agreement with the characteristic of n-type semiconductor.

Humidity is also an essential aspect to be considered for gas sensors in practical applications. The effect of humidity on the sensing performance of 6%Cu–In_2O_3 based sensor was investigated, as shown in Figs. 8(a) and 8(b). The response to 20 ppm H_2S shows a decreasing trend as the relative humidity is increased from 0 to 65%. This is due to the reduced interaction between the sensing material and H_2S gas, since more water molecules are adsorbed on the nanofiber surface under higher humidity, weakening the adsorption of H_2S on the sensing material [45,46]. In particular, the response still remains 29.3 (~60% of the initial value) as the relative humidity arrives at 65%, indicating that the 6%Cu–In_2O_3 based sensor can be used to detect H_2S under higher humidity.

Whether in scientific research or industrial production, the reproducibility and stability at the optimum operating temperature of sensors are essential for accurate monitoring of the target gas. Figure 8(c) illustrates the reproducibility of the 6%Cu–In_2O_3 based sensor for consecutive exposure and removal of 50 ppm H_2S (5 cycles), indicating that the sensor performs well in 5-cycle test with response of 350.7 ± 38.6 (Fig. 8(d)). The

sensor also has a good stability in sensing performance due to no obvious fluctuation in the variations of resistance and response/recovery rate during sensing. Moreover, the response of 6%Cu–In_2O_3 based sensor to 50 ppm H_2S for continuous 33 days presents a non-significant decrease (Fig. 8(e)), showing good long-term stability.

Table 1 lists the responses and response time of In_2O_3-based sensors to 50 and 100 ppm H_2S at ≥ 150 ℃ for sensing performance comparison. As shown in Table 1, the response of In_2O_3-based sensors to 50 ppm H_2S at 200–300 ℃ varies from 1.08 to 350.7, with the response time of ~2–60 s, indicating that the as-fabricated 6%Cu–In_2O_3 based sensor has the highest response to 50 ppm H_2S. Similarly, the response of 6%Cu–In_2O_3 based sensor to 100 ppm H_2S is far higher than those of other In_2O_3-based sensors except the comparable value of Mg–In_2O_3 nanotubes. In short, the as-fabricated 6%Cu–In_2O_3 based sensor has the highest response to H_2S under the comparable conditions compared with the reported In_2O_3-based sensors. Thus, the Cu–In_2O_3 hollow nanofibers fabricated by a combination of electrospinning and subsequent calcination have a promising application prospect in H_2S gas sensing.
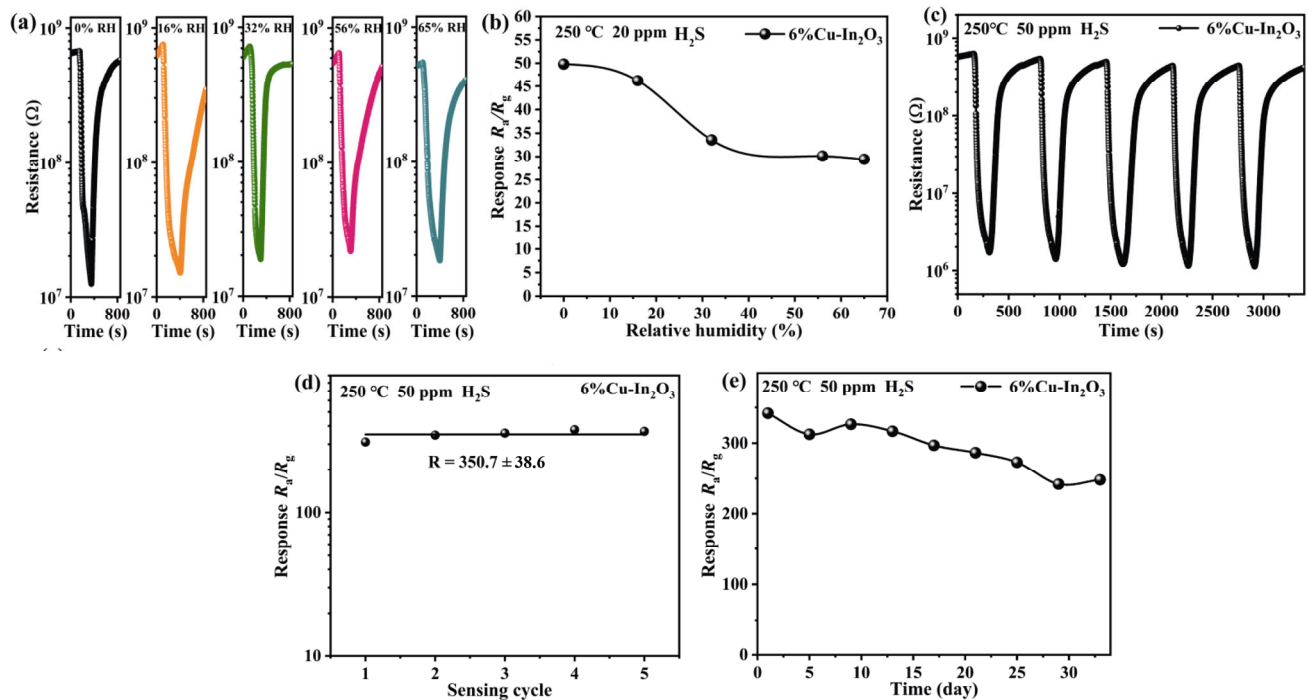
Fig. 8 (a, b) Responses of 6%Cu–In$_2$O$_3$ based sensor to 20 ppm H$_2$S at various relative humidity. (c, d) Reproducibility and (e) long-term stability of 6%Cu–In$_2$O$_3$ based sensor to 50 ppm H$_2$S at 250 ℃.

Table 1 Sensing performance comparison of In$_2$O$_3$-based sensors for 50 and 100 ppm H$_2$S at ≥ 150 ℃

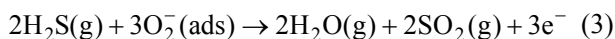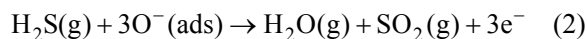| Material	Morphology	Temp. (℃)	Conc. (ppm)	Response R_a/R_g	τ_{res} (s)	Ref.
In$_2$O$_3$	Porous thin film	300	50	25	16	[47]
In$_2$O$_3$	Nanocubes	268.5	50	125	2	[48]
In$_2$O$_3$	Nanocrystals	270	50	149	2	[49]
In$_2$O$_3$	Nanocrystals	270	100	~185	2	[49]
ZnO/In$_2$O$_3$	Nanorods	300	50	~1.08	—	[50]
ZnO/In$_2$O$_3$	Nanorods	300	100	~1.1	750	[50]
La–In$_2$O$_3$	Hollow microspheres	200	50	50.3	~48	[25]
Pt–In$_2$O$_3$	Nanofibers	200	50	100	~60	[51]
Pt–In$_2$O$_3$	Nanofibers	200	100	~300	~60	[51]
Au–In$_2$O$_3$	Nanowires	300	50	301.5	35	[52]
Eu–In$_2$O$_3$	Nanobelts	260	100	5.74	11	[53]
Cu–In$_2$O$_3$	Hollow spheres	371	100	7.5	—	[54]
Pd–In$_2$O$_3$	Hollow spheres	371	100	8.7	—	[54]
Mg–In$_2$O$_3$	Nanotubes	150	100	2241.6	—	[55]
6%Cu–In$_2$O$_3$	Hollow nanofibers	250	50	350.7	24	This work
6%Cu–In$_2$O$_3$	Hollow nanofibers	250	100	4201.5	19	This work

3. 3 Sensing mechanism

There are many factors affecting the gas sensing behavior of 6%Cu–In$_2$O$_3$ based sensor, and the reasons for the improved sensing performance are mainly reflected in the following aspects.

(1) The increase of oxygen vacancy concentration derived from the Cu doping. The substitution of Cu^{2+} ions for In^{3+} ions can generate additional oxygen vacancies, and meanwhile defects involving oxygen vacancies can dominate the physical and chemical properties of oxide materials and serve as the preferred adsorption

sites for gas molecules [24,37]. So, the as-prepared Cu–In$_2$O$_3$ has great advantages in gas adsorption. Moreover, the doped hollow nanofibers have larger specific surface area, which can significantly promote surface interactions by providing more active adsorption sites, resulting in the enhancement of gas-sensitive response.

(2) The redox reactions occurred on the material surface.

(i) The reaction of adsorbed oxygen with H$_2$S. When the n-type In$_2$O$_3$ is exposed to air, O$_2$ in the air can capture electrons in the conduction band of In$_2$O$_3$ with certain energy, forming electron depletion layer on the surface. Under the operating temperature (250 ℃), there are mainly oxygen ions in the forms of O$^-$ and O$_2^-$ adsorbed on the 6%Cu–In$_2$O$_3$ nanofibers [9,56], so that the H$_2$S is oxidized to H$_2$O and SO$_2$ by the oxygen ions when exposed to H$_2$S (Fig. 9(a)), and meanwhile electrons are released. The sensing reactions are shown in Eqs. (2) and (3):

$$H_2S(g) + 3O^-(ads) \rightarrow H_2O(g) + SO_2(g) + 3e^- \quad (2)$$

$$2H_2S(g) + 3O_2^-(ads) \rightarrow 2H_2O(g) + 2SO_2(g) + 3e^- \quad (3)$$

The electrons are released into the conduction band of In$_2$O$_3$ in this process, so the resistance tends to decrease.

(ii) The reaction of CuO with H$_2$S. According to previous reports [29,57], CuO can be converted to Cu$_2$S when the 6%Cu–In$_2$O$_3$ based sensor is exposed to H$_2$S at a temperature of over 200 ℃. The resistance of the material can decrease rapidly because Cu$_2$S has high electrical conductivity, and the chemical reaction is shown in Eq. (4):

$$6CuO(s) + 4H_2S(g) \rightarrow 3Cu_2S(g) + 4H_2O(g) + SO_2(g) \quad (4)$$
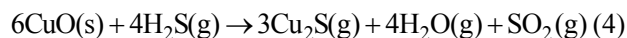
Once air is passed through to remove H$_2$S, Cu$_2$S will be oxidized slowly by the atmospheric oxygen and the resistance will begin to recover, the following reaction (Eq. (5)) will occur.

$$Cu_2S(s) + 2O_2(g) \rightarrow 2CuO(s) + SO_2(g) \quad (5)$$

However, the generation of too much Cu$_2$S can make the resistance difficult to recover to the original state in air, as a result of that the response tends to decrease when the Cu doping concentration exceeds 6%.

(3) Formation of p–n heterojunction. The electrons in In$_2$O$_3$ and holes in CuO flow in opposite directions due to the inhomogeneous carrier concentration as the p-type CuO is in contact with n-type In$_2$O$_3$ [58,59]. During this process, the energy band bends until the Fermi energy level (E_f) of the two materials reaches equilibrium, forming p–n heterojunctions with the electron depletion layer at the CuO/In$_2$O$_3$ interface (Fig. 9(b)). The p–n heterojunction can exhibit high resistance state, and offer a greater range of resistance drop for 6%Cu–In$_2$O$_3$ based sensor in H$_2$S gas, thus enhancing the gas sensing performance.
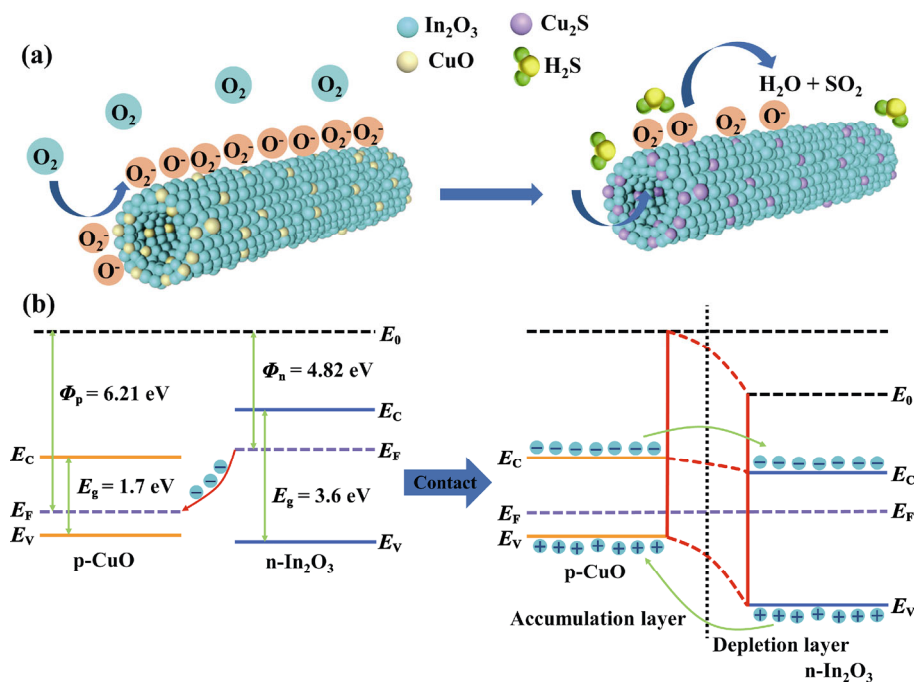

Fig. 9 Schematic illustrations of (a) the gas sensing mechanism of Cu-doped In$_2$O$_3$ nanofibers and (b) the formation of CuO/In$_2$O$_3$ heterojunction.

The first-principles calculations based on VASP were conducted with DFT to explain the gas adsorption mechanism of 6%Cu–In_2O_3(111) from the atomic scale. Although CuO can react with H_2S, here we ignore the role of CuO in the chemical reaction and only investigate the doping effect of Cu. We calculated the adsorption energies of the six gases with different atoms adsorbed on the In and Cu sites on the surface of the constructed model. Figures 10(a)–10(d) show the structural models with the adsorption energy for H_2S gas, and the other gas adsorption structural models are shown in Fig. S4 in the ESM. The calculated adsorption energies and charge transfer (Δq) of the six gases (H_2S, NO_2, SO_2, NH_3, ethanol, and acetone) on the surface of pristine In_2O_3(111) and 6%Cu–In_2O_3(111) nanofibers are listed in Fig. 10(e) and Table S1 in the ESM. Compared with the pristine In_2O_3 nanofibers, the adsorption energy of the four gas molecules (H_2S, NO_2, NH_3, and acetone) on the 6%Cu–In_2O_3(111) increase in varying degrees except the two comparable values of SO_2 and ethanol, and especially that of H_2S increases sharply from 2.22 to 3.88 eV, indicating that the gas adsorption capacity of H_2S gas is greatly enhanced by the Cu doping, which can contribute to the high response and selectivity. Moreover, from the perspective of charge transfer, H_2S

loses the maximum electron of 0.73e as donor to the 6%Cu–In_2O_3 when the target gas is adsorbed on the 6%Cu–In_2O_3(111) (Table S1 in the ESM), showing the highest response and good selectivity of 6%Cu–In_2O_3 to H_2S (Fig. 7(f)). However, the H_2S molecules are dissociated during the adsorption of H_2S on 6%Cu–In_2O_3 (Figs. 10(c) and 10(d)). This is because H_2S is strongly reductive and H_2S undergoes deprotonation reaction through the action of S atoms and Cu^{2+} to form HS and H [60], leading to the increase in the adsorption energy as well, which contributes to the high selectivity of 6%Cu–In_2O_3 to H_2S.

Moreover, the reason why the Cu doping can promote the sensing performance of In_2O_3 is explained. Actually, the gas adsorption can alter the work function (W) of materials. So, the work function induced by gas adsorption has become a promising way to describe the change of current densities to evaluate the sensor properties [61], and the current density in vacuum is described by [62]:

$$j = AT^2 \exp(-W/(kT))$$

where A, T, and W represent the Richardson constant (A/m^2), temperature (K), and work function (eV), respectively. There is a negative correlation between
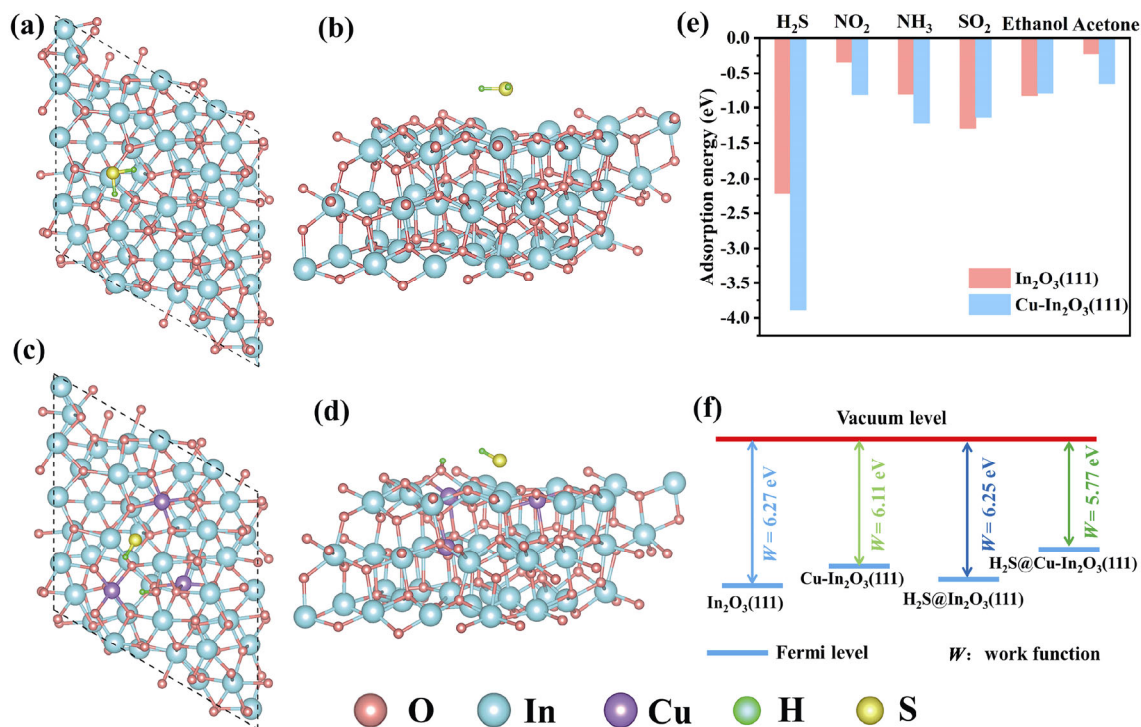

Fig. 10 Top and side views of the configurations for (a, b) H_2S adsorbed on In_2O_3(111), (c, d) H_2S adsorbed on 6%Cu–In_2O_3(111), obtained by DFT calculations. (e) Adsorption energy of different gas molecules adsorbed on In_2O_3(111) and 6%Cu–In_2O_3(111). (f) Work function of In_2O_3(111) and 6%Cu–In_2O_3(111) before and after H_2S adsorption.

the current density and work function. The calculated work functions are shown in Fig. 10(f), indicating that the work function of $In_2O_3(111)$ is 6.27 eV and that the work function reduces to 6.11 eV after Cu doping. So, it is easier for electrons to move from the inside to the surface of the substrate, which is benefit for gas adsorption of 6%Cu–$In_2O_3(111)$. When H_2S is adsorbed on $In_2O_3(111)$ ($H_2S@In_2O_3(111)$), the work function keeps basically unchanged. However, the work function decreases by 0.34 eV when H_2S is adsorbed on 6%Cu–$In_2O_3(111)$ ($H_2S@In_2O_3(111)$). Furthermore, the calculated DOSs indicate that the $In_2O_3(111)$ shows the semiconductor properties, with the bandgap of 0.76 eV (Fig. 11(a)). After the Cu doping, the bandgap of Cu–$In_2O_3(111)$ decreases to 0.11 eV (Fig. 11(b)), and much impurity levels are introduced around Fermi level (0 eV). When H_2S is adsorbed on $In_2O_3(111)$, the bandgap of $H_2S@In_2O_3(111)$ basically keeps consistent with that of $In_2O_3(111)$, only with the movement of the Fermi level, and the s orbit of H atom and p orbit of H atom only contribute to the deep levels of the valence band (Fig. 11(c)). Specially, when H_2S is adsorbed on Cu–$In_2O_3(111)$, a sharp peak appears at Fermi level due to the orbitals' hybridization of d orbital of Cu and

p orbital of S. Therefore, the Cu doping can promote the sensing performance of In_2O_3 to H_2S (Fig. 11(d)).

4 Conclusions

In this study, the pristine and Cu–In_2O_3 hollow nanofibers were prepared by a two-step method involving electrostatic spinning and annealing. A large portion of Cu^{2+} ions are doped into the In_2O_3 lattice and a small portion are applied to generate CuO while employing 6% Cu doping. The 6% Cu doping can make the surface of nanofibers smooth, homogenize and refine the diameter of nanofibers, increase the specific surface area to a certain extent, and especially enhance the formation of oxygen vacancies. Gas sensing experiments and DFT calculations (involving the adsorption energy, work function, and DOS) demonstrate the excellent selectivity and sensing performance of 6% Cu-doped In_2O_3 to H_2S. The response of 6%Cu–In_2O_3 sensor can reach 350.7 and 4201.5 to 50 and 100 ppm H_2S at the optimum operation temperature of 250 ℃, and the response time is only 24 and 19 s, respectively. In particular, the response of 6%Cu–In_2O_3 sensor to 1 ppm
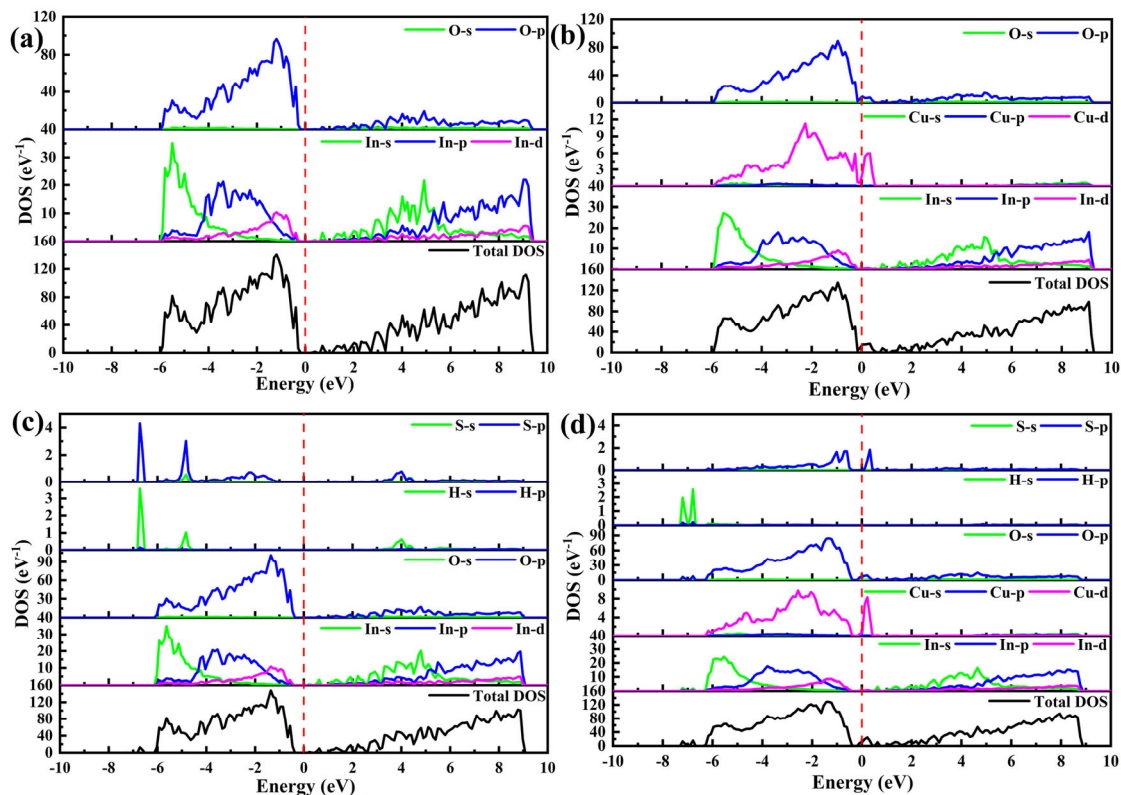

Fig. 11 Density of states of (a) pristine $In_2O_3(111)$, (b) 6%Cu–$In_2O_3(111)$, (c) $H_2S@In_2O_3(111)$, and (d) $H_2S@6$%Cu– $In_2O_3(111)$. The red dotted line represents the Fermi level.

H_2S reaches 1.5. Moreover, its response to 20 ppm H_2S gradually decreases from ~50 to 30 with the relative humidity increasing from 0 to 65%. The 6%Cu–In_2O_3 hollow nanofiber based sensor presents excellent sensing performance to H_2S gas owing to the following aspects: (1) the increase of oxygen vacancy concentration derived from the Cu doping; (2) the redox reactions of adsorbed oxygen and CuO with H_2S on the material surface; and (3) the formation of p–n heterojunction. This work can provide a promising approach to achieve high-performance In_2O_3-based gas sensor for H_2S detection.

Acknowledgements

Electronic Supplementary Material

Supplementary material is available in the online version of this article at https://doi.org/10.1007/s40145-021-0546-2.

References

[1] Kumar V, Majhi SM, Kim KH, *et al*. Advances in In_2O_3-based materials for the development of hydrogen sulfide sensors. *Chem Eng J* 2021, **404**: 126472.

[2] Ali FIM, Awwad F, Greish YE, *et al*. Hydrogen sulfide (H_2S) gas sensor: A review. *IEEE Sens J* 2019, **19**: 2394–2407.

[3] Mirzaei A, Kim SS, Kim HW. Resistance-based H_2S gas sensors using metal oxide nanostructures: A review of recent advances. *J Hazard Mater* 2018, **357**: 314–331.

[4] Annanouch FE, Haddi Z, Vallejos S, *et al*. Aerosol-assisted CVD-grown WO_3 nanoneedles decorated with copper oxide nanoparticles for the selective and humidity-resilient detection of H_2S. *ACS Appl Mater Interfaces* 2015, **7**: 6842–6851.

[5] Zhu LY, Yuan KP, Yang JH, *et al*. Hierarchical highly ordered SnO_2 nanobowl branched ZnO nanowires for ultrasensitive and selective hydrogen sulfide gas sensing. *Microsyst Nanoeng* 2020, **6**: 30.

[6] Wang MS, Luo Q, Hussain S, *et al*. Sharply-precipitated

[7] Reja SI, Sharma N, Gupta M, *et al*. A highly selective fluorescent probe for detection of hydrogen sulfide in living systems: *In vitro* and *in vivo* applications. *Chem A Eur J* 2017, **23**: 9872–9878.

[8] Zhu L, Zeng W. Room-temperature gas sensing of ZnO-based gas sensor: A review. *Sens Actuat A*: *Phys* 2017, **267**: 242–261.

[9] Ma JW, Fan HQ, Zheng XK, *et al*. Facile metal-organic frameworks-templated fabrication of hollow indium oxide microstructures for chlorine detection at low temperature. *J Hazard Mater* 2020, **387**: 122017.

[10] Li R, Chen S, Lou Z, *et al*. Fabrication of porous SnO_2 nanowires gas sensors with enhanced sensitivity. *Sens Actuat B*: *Chem* 2017, **252**: 79–85.

[11] Liu SW, Wang MY, Liu GW, *et al*. Enhanced NO_2 gas-sensing performance of 2D Ti_3C_2/TiO_2 nanocomposites by *in situ* formation of Schottky barrier. *Appl Surf Sci* 2021, **567**: 150747.

[12] Chethana DM, Thanuja TC, Mahesh HM, *et al*. Synthesis, structural, magnetic and NO_2 gas sensing property of CuO nanoparticles. *Ceram Int* 2021, **47**: 10381–10387.

[13] Liu D, Ren XW, Li YS, *et al*. Nanowires-assembled WO_3 nanomesh for fast detection of ppb-level NO_2 at low temperature. *J Adv Ceram* 2020, **9**: 17–26.

[14] Wang MS, Jin CC, Luo Q, *et al*. Sol-gel derived TiO_2–carbon composites with adsorption-enhanced photocatalytic activity and gas sensing performance. *Ceram Int* 2020, **46**: 18608–18613.

[15] Xiong Y, Tang ZL, Wang Y, *et al*. Gas sensing capabilities of TiO_2 porous nanoceramics prepared through premature sintering. *J Adv Ceram* 2015, **4**: 152–157.

[16] Tan J, Hussain S, Ge CX, *et al*. ZIF-67 MOF-derived unique double-shelled Co_3O_4/$NiCo_2O_4$ nanocages for superior gas-sensing performances. *Sens Actuat B*: *Chem* 2020, **303**: 127251.

[17] Ma JW, Fan HQ, Zhao N, *et al*. Synthesis of In_2O_3 hollow microspheres for chlorine gas sensing using yeast as bio-template. *Ceram Int* 2019, **45**: 9225–9230.

[18] Song LF, Dou KP, Wang RR, *et al*. Sr-doped cubic In_2O_3/rhombohedral In_2O_3 homojunction nanowires for highly sensitive and selective breath ethanol sensing: Experiment and DFT simulation studies. *ACS Appl Mater Interfaces* 2020, **12**: 1270–1279.

[19] Liu W, Xie YL, Chen TX, *et al*. Rationally designed mesoporous In_2O_3 nanofibers functionalized Pt catalysts for high-performance acetone gas sensors. *Sens Actuat B*: *Chem* 2019, **298**: 126871.

[20] Araújo ES, Leão VNS. TiO_2/WO_3 heterogeneous structures prepared by electrospinning and sintering steps: Characterization and analysis of the impedance variation to humidity. *J Adv Ceram* 2019, **8**: 238–246.

[21] Shen YB, Zhong XX, Zhang J, *et al*. *In-situ* growth of

mesoporous In_2O_3 nanorod arrays on a porous ceramic substrate for ppb-level NO_2 detection at room temperature. *Appl Surf Sci* 2019, **498**: 143873.

[22] Tao ZH, Li YW, Zhang B, *et al*. Synthesis of urchin-like In_2O_3 hollow spheres for selective and quantitative detection of formaldehyde. *Sens Actuat B*: *Chem* 2019, **298**: 126889.

[23] Zeng XG, Li S, He Y, *et al*. Gas sensors based on pearl-necklace-shaped In_2O_3 nanotubes with highly enhanced formaldehyde-sensing performance. *J Mater Sci*: *Mater Electron* 2019, **30**: 18362–18373.

[24] Zhao CH, Gong HM, Niu GQ, *et al*. Electrospun Ca-doped In_2O_3 nanotubes for ethanol detection with enhanced sensitivity and selectivity. *Sens Actuat B*: *Chem* 2019, **299**: 126946.

[25] Wei DD, Jiang WH, Gao HY, *et al*. Facile synthesis of La-doped In_2O_3 hollow microspheres and enhanced hydrogen sulfide sensing characteristics. *Sens Actuat B*: *Chem* 2018, **276**: 413–420.

[26] Sun YJ, Zhao ZT, Suematsu K, *et al*. Rapid and stable detection of carbon monoxide in changing humidity atmospheres using clustered In_2O_3/CuO nanospheres. *ACS Sens* 2020, **5**: 1040–1049.

[27] Li SH, Xie LL, He M, *et al*. Metal-organic frameworks-derived bamboo-like CuO/In_2O_3 heterostructure for high-performance H_2S gas sensor with Low operating temperature. *Sens Actuat B*: *Chem* 2020, **310**: 127828.

[28] Liang XS, Kim TH, Yoon JW, *et al*. Ultrasensitive and ultraselective detection of H_2S using electrospun CuO-loaded In_2O_3 nanofiber sensors assisted by pulse heating. *Sens Actuat B*: *Chem* 2015, **209**: 934–942.

[29] Park KR, Cho HB, Lee J, *et al*. Design of highly porous SnO_2–CuO nanotubes for enhancing H_2S gas sensor performance. *Sens Actuat B*: *Chem* 2020, **302**: 127179.

[30] Momma K, Izumi F. VESTA 3 for three-dimensional visualization of crystal, volumetric and morphology data. *J Appl Cryst* 2011, **44**: 1272–1276.

[31] Perdew JP, Burke K, Ernzerhof M. Generalized gradient approximation made simple. *Phys Rev Lett* 1996, **77**: 3865–3868.

[32] Grimme S. Accurate description of van der Waals complexes by density functional theory including empirical corrections. *J Comput Chem* 2004, **25**: 1463–1473.

[33] Seixas L, Carvalho A, Castro Neto AH. Atomically thin dilute magnetism in Co-doped phosphorene. *Phys Rev B* 2015, **91**: 155138.

[34] Wang MY, Li LH, Zhao GH, *et al*. Influence of the surface decoration of phosphorene with Ag nanoclusters on gas sensing properties. *Appl Surf Sci* 2020, **504**: 144374.

[35] Vikrant K, Kumar V, Ok YS, *et al*. Metal-organic framework (MOF)-based advanced sensing platforms for the detection of hydrogen sulfide. *TrAC Trends Anal Chem* 2018, **105**: 263–281.

[36] Zhang C, Huan YC, Sun DJ, *et al*. Synthesis and NO_2 sensing performances of CuO nanoparticles loaded In_2O_3 hollow spheres. *J Alloys Compd* 2020, **842**: 155857–155866.

[37] Koo BR, Oh ST, Ahn HJ. Camphene effect for morphological change of electrospun SnO_2 nanofibres: From dense to fibre-in-hollow and to hollow nanostructures. *Mater Lett* 2016, **178**: 288–291.

[38] Zhang XL, Song DL, Liu Q, *et al*. Designed synthesis of Ag-functionalized Ni-doped In_2O_3 nanorods with enhanced formaldehyde gas sensing properties. *J Mater Chem C* 2019, **7**: 7219–7229.

[39] Zhou JY, Bai JL, Zhao H, *et al*. Gas sensing enhancing mechanism via doping-induced oxygen vacancies for gas sensors based on indium tin oxide nanotubes. *Sens Actuat B*: *Chem* 2018, **265**: 273–284.

[40] Liang QH, Zou XX, Chen H, *et al*. High-performance formaldehyde sensing realized by alkaline-earth metals doped In_2O_3 nanotubes with optimized surface properties. *Sens Actuat B*: *Chem* 2020, **304**: 127241.

[41] Bai JL, Wang Q, Wang YR, *et al*. Role of nickel dopant on gas response and selectivity of electrospun indium oxide nanotubes. *J Colloid Interface Sci* 2020, **560**: 447–457.

[42] Ri JS, Li XW, Shao CL, *et al*. Sn-doping induced oxygen vacancies on the surface of the In_2O_3 nanofibers and their promoting effect on sensitive NO_2 detection at low temperature. *Sens Actuat B*: *Chem* 2020, **317**: 128194.

[43] Wan K, Wang D, Wang F, *et al*. Hierarchical In_2O_3@SnO_2 core–shell nanofiber for high efficiency formaldehyde detection. *ACS Appl Mater Interfaces* 2019, **11**: 45214–45225.

[44] Vuong NM, Chinh ND, Huy BT, *et al*. CuO-decorated ZnO hierarchical nanostructures as efficient and established sensing materials for H_2S gas sensors. *Sci Rep* 2016, **6**: 26736.

[45] Chen KX, Lu H, Li G, *et al*. Surface functionalization of porous In_2O_3 nanofibers with Zn nanoparticles for enhanced low-temperature NO_2 sensing properties. *Sens Actuat B*: *Chem* 2020, **308**: 127716.

[46] Hittini W, Abu-Hani AF, Reddy N, *et al*. Cellulose-Copper Oxide hybrid nanocomposites membranes for H_2S gas detection at low temperatures. *Sci Rep* 2020, **10**: 2940.

[47] Wang YY, Duan GT, Zhu YD, *et al*. Room temperature H_2S gas sensing properties of In_2O_3 micro/nanostructured porous thin film and hydrolyzation-induced enhanced sensing mechanism. *Sens Actuat B*: *Chem* 2016, **228**: 74–84.

[48] Xu JQ, Wang XH, Shen JN. Hydrothermal synthesis of In_2O_3 for detecting H_2S in air. *Sens Actuat B*: *Chem* 2006, **115**: 642–646.

[49] Xu JQ, Wang XH, Li C. Electrochemical-deposited In_2O_3 nanocrystals for H_2S detecting in air. *Electrochem Solid-State Lett* 2006, **9**: H53.

[50] Park S, Kim H, Jin C, *et al*. Enhanced gas sensing properties of multiple networked In_2O_3-core/ZnO-shell nanorod sensors. *J Nanosci Nanotechnol* 2013, **13**: 3427–3432.

[51] Zheng W, Lu XF, Wang W, *et al*. Assembly of Pt nanoparticles on electrospun In_2O_3 nanofibers for H_2S detection. *J Colloid Interface Sci* 2009, **338**: 366–370.

[52] Liu B, Xu YM, Li K, *et al*. Pd-catalyzed reaction-producing

intermediate S on a Pd/In$_2$O$_3$ surface: A key to achieve the enhanced CS$_2$-sensing performances. *ACS Appl Mater Interfaces* 2019, **11**: 16838–16846.

[53] Chen WW, Liu YK, Qin ZJ, *et al*. A single Eu-doped In$_2$O$_3$ nanobelt device for selective H$_2$S detection. *Sensors* 2015, **15**: 29950–29957.

[54] Kim SJ, Hwang IS, Kang YC, *et al*. Design of selective gas sensors using additive-loaded In$_2$O$_3$ hollow spheres prepared by combinatorial hydrothermal reactions. *Sensors*: *Basel* 2011, **11**: 10603–10614.

[55] Zhao CH, Huang BY, Xie EQ, *et al*. Improving gas-sensing properties of electrospun In$_2$O$_3$ nanotubes by Mg acceptor doping. *Sens Actuat B*: *Chem* 2015, **207**: 313–320.

[56] Wang C, Wang W, He K, *et al*. Pr-doped In$_2$O$_3$ nanocubes induce oxygen vacancies for enhancing triethylamine gas-sensing performance. *Front Mater Sci* 2019, **13**: 174–185.

[57] Ma LG, Ai XQ, Lu YZ, *et al*. Facile and novel *in situ* low-temperature growth of Cu$_2$S nanoarrays based on Cu substrates. *Appl Phys A* 2019, **125**: 373.

[58] Boroun Z, Ghorbani M, Mohammadpour R, *et al*. Importance of N–P–N junction in H$_2$S sensing process of SnO$_2$–CuO heterostructures: A theoretical macroscopic approach. *IEEE Sens J* 2021, **21**: 7123–7129.

[59] Sun LM, Zhuang Y, Yuan YS, *et al*. Nitrogen-doped carbon-coated CuO–In$_2$O$_3$ p–n heterojunction for remarkable photocatalytic hydrogen evolution. *Adv Energy Mater* 2019, **9**: 1902839.

[60] Sun SJ, Zhang DS, Li CY, *et al*. DFT study on the adsorption and dissociation of H$_2$S on CuO(111) surface. *RSC Adv* 2015, **5**: 21806–21811.

[61] Stegmeier S, Fleischer M, Tawil A, *et al*. Sensing mechanism of room temperature CO$_2$ sensors based on primary amino groups. *Sens Actuat B*: *Chem* 2011, **154**: 270–276.

[62] Beheshtian J, Peyghan AA, Bagheri Z. Detection of phosgene by Sc-doped BN nanotubes: A DFT study. *Sens Actuat B*: *Chem* 2012, **171–172**: 846–852.